Baghdad Science Journal

Volume 22 | Issue 3 Article 18

3-24-2025

Synthesis and Photocatalytic Applications of TiO_2-CQDs Nanocomposites Prepared by Biological Methods

Maryam S. Jabbar
Department of Physics, College of Science, University of Diyala, Diyala, Iraq, sciphdr07@uodiyala.edu.iq

Olfat A. Mahmood
Department of Physics, College of Science, University of Diyala, Diyala, Iraq, Olfat@uodiyala.edu.iq

Zainab N. Jameel
Communication Engineering Department, University of Technology, Baghdad, Iraq,
zainab.n.jameel@uotechnology.edu.iq

Noor J. Jihad
Communication Engineering Department, University of Technology, Baghdad, Iraq,
NOOR.J.JIHAD@uotechnology.edu.iq

How to Cite this Article

Jabbar, Maryam S.; Mahmood, Olfat A.; Jameel, Zainab N.; and Jihad, Noor J. (2025) "Synthesis and Photocatalytic Applications of TiO_2-CQDs Nanocomposites Prepared by Biological Methods," *Baghdad Science Journal*: Vol. 22: Iss. 3, Article 18.
DOI: https://doi.org/10.21123/bsj.2024.9549

BAGHDAD SCIENCE JOURNAL 2025;22(3):923–937

RESEARCH ARTICLE

Synthesis and Photocatalytic Applications of TiO_2-CQDs Nanocomposites Prepared by Biological Methods

Maryam S. Jabbar [1], **Olfat A. Mahmood** [1], **Zainab N. Jameel** [2], **Noor. J. Jihad** [2,*]

[1] Department of Physics, College of Science, University of Diyala, Diyala, Iraq
[2] Communication Engineering Department, University of Technology, Baghdad, Iraq

ABSTRACT

In this study, CQDs were synthesized by the green method using orange juice and ethanol, confused at a relatively low temperature by hydrothermal carbonization process, TiO_2 were prepared by a facile sol-gel method, and TiO_2-CQDs nanocomposites with different weight ratios were prepared by slipe mixing and heat treatment. XRD showed that the CQDs exhibited a broad peak at (002) with hexagonal structure, and TiO_2 (anatase phase) had a polycrystalline nature with tetragonal structure. The FESEM results showed the formation of nanostructures with different shapes and small average particle size. High-resolution transmission electron microscopy revealed that the TiO_2 (anatase phase) agglomerated in mostly spherical shapes and sizes less than 15 nm. The CQDs had a relatively uniform diameter, a spherical shape with a highly crystalline structure, and a size below 5 nm. The FTIR spectra of TiO_2 NPs, CQDs, and TiO_2-CQDs nanocomposite showed the presence of a broad band at 450–4000 cm^{-1}, which corresponded to the stretching vibration of terminating hydroxyl groups in samples. The results of UV-visible spectroscopy showed that the absorbance of TiO_2-CQDs nanocomposite increased with the increase in the CQDs rate, and the optical energy band gap of TiO_2 and CQDs was 3.14 ev and 3.07 eV, respectively. The energy band gap values of TiO_2-CQDs nanocomposite decreased with the increase in the CQDs rate in the range of (2.72–1.85) eV. The performance of the Photocatalytic was shown by decreasing methylene blue (MB) and methyl orange (MO) under UV irradiation. The results showed that the TiO_2-CQDs nanocomposite with different weight ratios had higher photocatalytic efficiency than TiO_2 NPs, and the photocatalytic efficiency increased with the increase in the CQDs rate. The degradation efficiencies of MB and MO were high at 84% and 39% within 240 min, respectively.

Keywords: Anatase, Carbon quantum dots (CQDs), Field emission scanning electron microscopy (FESEM), High-resolution transmission electron microscopy (HRTEM), Titanium oxide (TiO_2), X-Ray diffraction (XRD)

Introduction

Nanocomposites are a type of composite material with at least one of their phases exhibiting dimensions in the nanometer range (1 nm = 10–9 m). Nanocomposite materials have emerged as a suitable alternative to overcome the limitations of micro composites and monolithic, despite posing preparation challenges related to the control of elemental composition and stoichiometry in the nanocluster phase.[1] Titanium dioxide (TiO_2) nanoparticles (NPs) with a diameter of no more than 100 nm have been developed into a novel component of innovative materials as a result of their own visual properties, dielectric behavior, and photocatalytic characteristic as a quantization of size.[2] TiO_2 is regarded as an active photocatalyst, and it is used in many applications as a self-cleaning and self-sanitizing component of

---

Received 19 September 2023; revised 18 February 2024; accepted 20 February 2024.

* Corresponding author.
E-mail addresses: sciphdr07@uodiyala.edu.iq (M. S. Jabbar), Olfat@uodiyala.edu.iq (O. A. Mahmood), zainab.n.jameel@uotechnology.edu.iq (Z. N. Jameel), NOOR.J.JIHAD@uotechnology.edu.iq (N. J. Jihad).

https://doi.org/10.21123/bsj.2024.9549

exterior coverings.[3] In addition, it can be utilized to clean the environment because it is non-toxic and has superior hydrophobicity and anti-fogging influence. These characteristics are extremely useful in removing bacteria and other harmful biological material found in air and water. In can also be utilized as a self-cleaning or self-sterilizing exterior for spaces such as medical care centers.[4] TiO_2 has been utilized in various applications because of its extreme stability, low cost, biocapacity, and reusability. Some examples of these applications include photocatalysis, the reinforcement of catalysts, antibacterial treatment, environmentally friendly remediation, cleansing of air, and purification of water.[5] TiO_2 exerts a powerful oxidizing influence, so it can be used to kill microorganisms when exposed to ultraviolet (UV) light with sufficient brightness.[6,7] TiO_2 NPs have found applications in biology, the pharmaceutical industry, and environmental protection in recent decades due to their antibacterial properties. For instance, TiO_2NPs have been used in photocatalysts and gas sensors. Moreover, they have been used in a variety of commercial and industrial applications, including solar cell and nutrient technology, ointments, toothpaste, pigment, cosmetics, and paints.[8] Carbon quantum dots (CQDs) are a newly developed family of carbon-related substances that, in contrast to transition metal semiconductor QDs, are nontoxic, biocompatible, and ecologically benign. Additionally, because to quantum confinement phenomena, CQDs show substantial size and excitation wavelength dependent photoluminescence (PL) features.[9–11] Given the presence of a large number of emissive traps on the surface of bare CQDs, the PL quantum yield of these particles is typically quite low. This feature represents a significant limitation in the field of lighting, including bioimaging, PL analysis, and light-emitting diodes (LEDs).[12–15] Thus, to increase brightness, CQDs' surface has to be passivated.[16] However, it has been shown that electrons may quickly accept and transport through carbon nanomaterials. These characteristics offer a very effective technique to regulate the movement of photoinduced charge carriers.[17,18] Effective solar energy harvesting and the prevention of recombination of charge carriers are two essential components of semiconductor-based photocatalysis.[19] By creating a heterojunction system out of CQDs and semiconductors, the properties of CQDs, such as their high coefficient of absorption and quick electron transport, may be exploited to increase the photocatalytic performance.[20,21] Many extremely powerful catalysts that use CQDs have been developed, including CQD/TiO_2.[22] Examples are CQD/SiO_2[23] and CQD/Fe_2O_3.[24] Meanwhile, a special PL characteristic of CQDs, has just been reported. By consecutively absorbing two or more photons over long wavelengths, this feature can convert low-energy photons into photons with high energy over CQDs.[25,26] A nanocomposite of CQDs and TiO_2 is to efficiently use the full spectrum of sunlight. and the modification of TiO_2 as a photocatalytic antibacterial material that will work effectively under visible sunlight. CQDs have the ability to reduce the band gap of semiconductor materials so that more reactive oxygen species can be generated by light, thus increasing the photocatalytic reactions and improving the degradation efficiency of bacteria[27] and CQD-modified TiO_2 composite material may exhibit sustainable antibacterial properties due to the formation of a new chemical bond (Ti-O-C) with a "dyade" structure.[28] And the CQDs/TiO_2 composites demonstrate the common features of narrow band gap, enhanced absorption of visible light, and prolonged lifetime of excited electrons and holes, which significantly improve the photocatalytic performance in degrading various water pollutants.[29] carbon quantum dots (CQDs) modified TiO_2 photocatalysts were successfully prepared by a facile sol-gel method. and photocatalytic performance was tested by degrading methylene blue (MB) under visible light irradiation. The degradation efficiency of methylene blue (MB) is as high as 90% within 120 min, which is 3.6 times higher than that of pure TiO_2.[30] In this article, we present a straight forward sol-gel approach for linking up conversion CQDs and TiO_2 microspheres, which enhances the photocatalytic activity of organic dyes (methylene blue [MB] and methyl orange [MO]) when exposed to UV light.

Experimental details

Synthesis of TiO_2 NP powder via the sol-gel method

As initial building blocks, we made use of titanium tetrachloride ($TiCl_4$) with a purity of 99.99% and ethanol (CH_3CH_2OH) with a purity of 99.99%. The synthesis procedure was completed by introducing a series of droplets derived from $TiCl_4$ into absolute ethanol solution at a ratio of 1:10. At room temperature, the reaction was carried out by utilizing a magnetic stirrer inside of a chemical fume hood to release unwanted toxic gases, specifically HCl. The formation procedure resulted in the production of a pale-yellow solution that had a pH of 1.4–2. After subjecting the obtained solution to 80 °C for 12 h, the gel state was successfully achieved. Calcination was performed to achieve the anatase phase for TiO_2. Under 450 °C for 1.5 h, the anatase phase was produced.

Synthesis of CQDs via the green method

CQDs are made through a process called hydrothermal carbonization, which involves mixing ethanol with natural raw materials and carbonizing the mixture at a relatively low temperature. The hydrothermal carbonization process creates CQDs largely by dehydrating, polymerizing, and carbonizing tiny, non-conjugated molecules like those in orange juice (citric acid, glucose, sucrose, fructose, and ascorbic acid). The requisite amounts of ethanol and pulp-free orange juice were mixed in the mixer to create a yellow solution. The glass bowl holding the solution was placed inside an autoclave made of stainless steel and then completely sealed off. The temperature was set to approximately 120 °C, and only one atmosphere was inside the autoclave. The process was completed in approximately 150 min. After the allotted time had passed, the autoclave was turned off and allowed to gradually cool down at room temperature. Subsequently, 40 mL of the dark brown solution was extracted. The solution was centrifuged and washed using dichloromethane and an abundant amount of acetone to obtain liquid and deposit, which were then separated from each other. The deposit was dried, and the powder that was formed from the CQDs was the deposit after it dried.

Synthesis of TiO_2-CQD nanocomposite

TiO_2-CQD nanocomposites were synthesized by slipe mixing and heat treatment method. Four combinations of composites were prepared by mixing 0.3 g of TiO_2 (anatase phase) and various quantities of CQDs (0.1, 0.3, 0.7 and 1% (w/w)). Each of the mixtures were added to 20 mL of deionized water, stirred for 3 h, and dried in an oven at 80 °C for 12 h. They were characterized and analyzed by using an FTIR fluorescence spectrophotometer and UV–Vis spectrophotometer.

Photocatalytic activity

Monitoring the degradation of MB dye as a model pollutant served as the basis for determining how effective the synthesized photo-catalyst samples were. For optimal control of photocatalytic degradation, the optical absorption peak of MB dye should be set at 664.5 nm. A magnetic stirrer was used to mix the solution for 2 h after 10 mg of MB was dissolved in 1000 mL of DW. Approximately 50 mg of TiO_2 and TiO_2-CQD nanocomposite with different weight ratios was added to 50 mL of MB (10 mg/mL) and then stirred in a dark room for 60 min to allow adsorption equilibrium between MB and catalyst surfaces. The solution was then irradiated by using a UV lamp with a power output of 6 W and a wavelength of 254 nm. The samples were removed after an equal amount of time had passed 60 min, filtered, and monitored by UV-Visible spectroscopy (using a Shimadzu 1900i-Jaban) to determine the degree to which the MB dye had degraded according to the following equation:[31]

$$\text{Efficiency} = \frac{(C_0 - C)}{C_0} \times 100\% = \frac{(A_0 - A)}{A_0} \times 100\% \quad (1)$$

where C_0, C, A_0, and A are the concentration of MB before and after illumination with UV light. The same procedure was used for MO dye, but the wavelength of MO was about 473 nm.

Results and discussion

X-ray diffraction analysis

X-ray diffraction (XRD) analysis was conducted to determine the structure of TiO_2 NPs. The crystal type in the spectrum was found to be anatase when heated to 450 °C, as shown in Fig. 1a. The intensity peaks of TiO_2 (anatase phase) have a polycrystalline nature with tetragonal structure oriented at diffraction angles 2θ at 25.52°, 37.04°, 38.01°, 38.67°, 48.23°, 54.09°, 55.26°, 62.87°, 68.95°, 70.43°, and 75.25° with diffraction planes of (101), (103), (004), (112), (200), (105), (211), (204), (116), (220), and (215), respectively. These findings were in line with the card number that was given out by the International Center for Diffraction Data (ICDD), which was 21-1272, and they were comparable with those found in other studies.[32,33]

In this investigation, Scherrer's formula was utilized to determine the crystallite size:[32]

$$D = 0.9\lambda / (\beta \cos\theta) \quad (2)$$

where D is the crystallite size, λ is the X-ray wavelength of CuKα line radiation, β is the full width at half maximum, θ is Bragg's angle, and the crystallite size for TiO_2 (anatase phase) is 15.89 nm as shown in the Table 1. The XRD pattern in Fig. 1b of the CQDs showed a broad peak at 19.42°, which corresponded to the (002) hkl plane with hexagonal structure, this result was in agreement with (ICDD) card number (48-1206) and comparable with those reported by other studies.[34,35] The crystallite size of the CQDs was 1.28 nm as shown in the T Table 1.

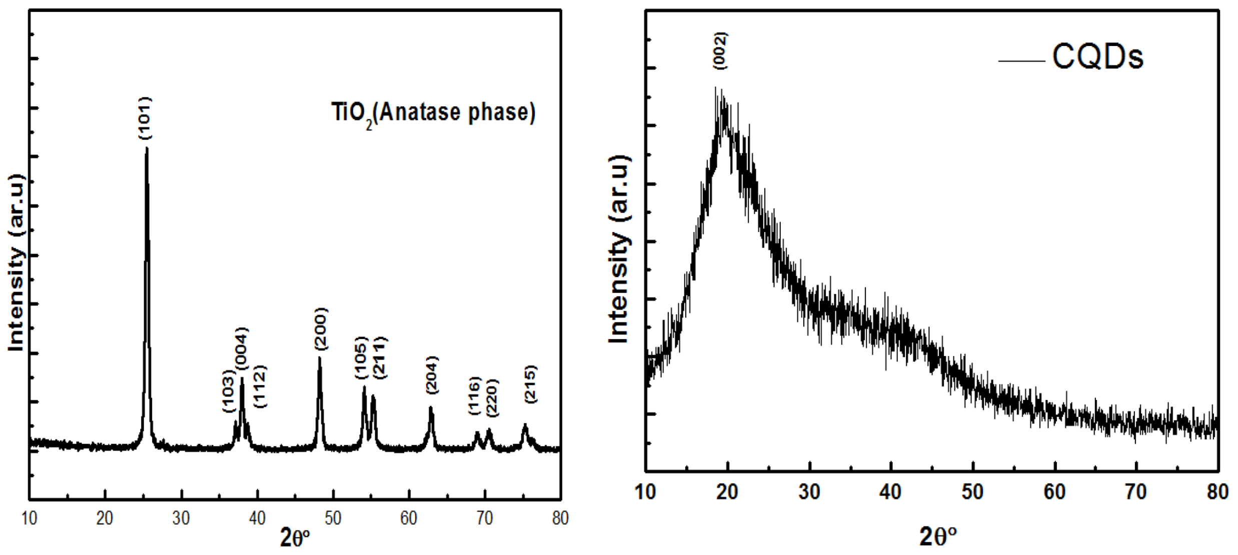

(a) **(b)**

Fig. 1. X-ray diffraction patterns of TiO_2 (a) and of CQDs (b).

Table 1. Structural parameters of the TiO_2 and CQDs.

Sample	TiO_2 (anatase phase)	CQDs
hkl	101	002
2θ (deg)	25.52	19.42
d_{hkl} (Å)	3.4874	4.5660
FWHM (deg)	0.4878	6.1200
Lattice constant (a_o) (Å)	3.77	10.54
Lattice constant (c_o) (Å)	9.48	17.23
Volume of cell (Å^3)	134.73	1657.66
D (nm)	15.89	1.28

The interplanar spacing (d) was calculated using Bragg's equation.[36]

$$n\lambda = 2d \sin\theta \tag{3}$$

Add to the lattice constants for the tetragonal structure of TiO_2 can be calculated according to the following equation:[37]

$$\frac{1}{d^2} = \frac{h^2+k^2}{a^2} + \frac{l^2}{c^2} \tag{4}$$

And for hexagonal unit cell of CQDs, the lattice constants (a_o, c_o) are given by:[36]

$$\frac{1}{d^2} = \frac{4}{3}\left(\frac{h^2+hk+k^2}{a^2}\right) + \frac{l^2}{c^2} \tag{5}$$

Where (h, k, l) are the Miller indices. The cell volume (v) was calculated for TiO_2 and CQDs according to the following equations sequentially:[38]

$$V = {a_o}^2 c_o \tag{6}$$

$$V = \sqrt{3}/2{a_o}^2 c_o \tag{7}$$

From the Table 1, it is clear that the values of the lattice constants and The cell volume of TiO_2 and CQDs are in agreement with the values of the (ICDD) standard cards for both materials; (a_o = 3.78 Å, c_o = 9.51 Å, V = 136.31 Å^3) and (a_o = 10.59 Å, c_o = 17.26 Å, V = 1677.62 Å^3); respectively.

Field-emission scanning electron microscopy analysis

Field-emission scanning electron microscopy (FESEM), which provides precise, high-magnification surface scans, was performed to study the surface topography of the prepared material. The images of all of the prepared materials, magnified at a ratio of 135KX to 70KX, are displayed in the figures. The TiO_2 NPs (anatase phase) had Cauliflower-like, in agreement with other studies.[33,39] The average particle size of TiO_2 NPs was 36.9 nm, as illustrated in Fig. 2(a).

The images of the CQDs in Fig. 2(b) showed the formation of nanostructures, they grew under self-assembly and exhibited small spherical structures under hydrothermal conditions. These results concurred with those of previous research' findings.[40] The average particle size of CQD NPs was determined to be 15.2 nm.

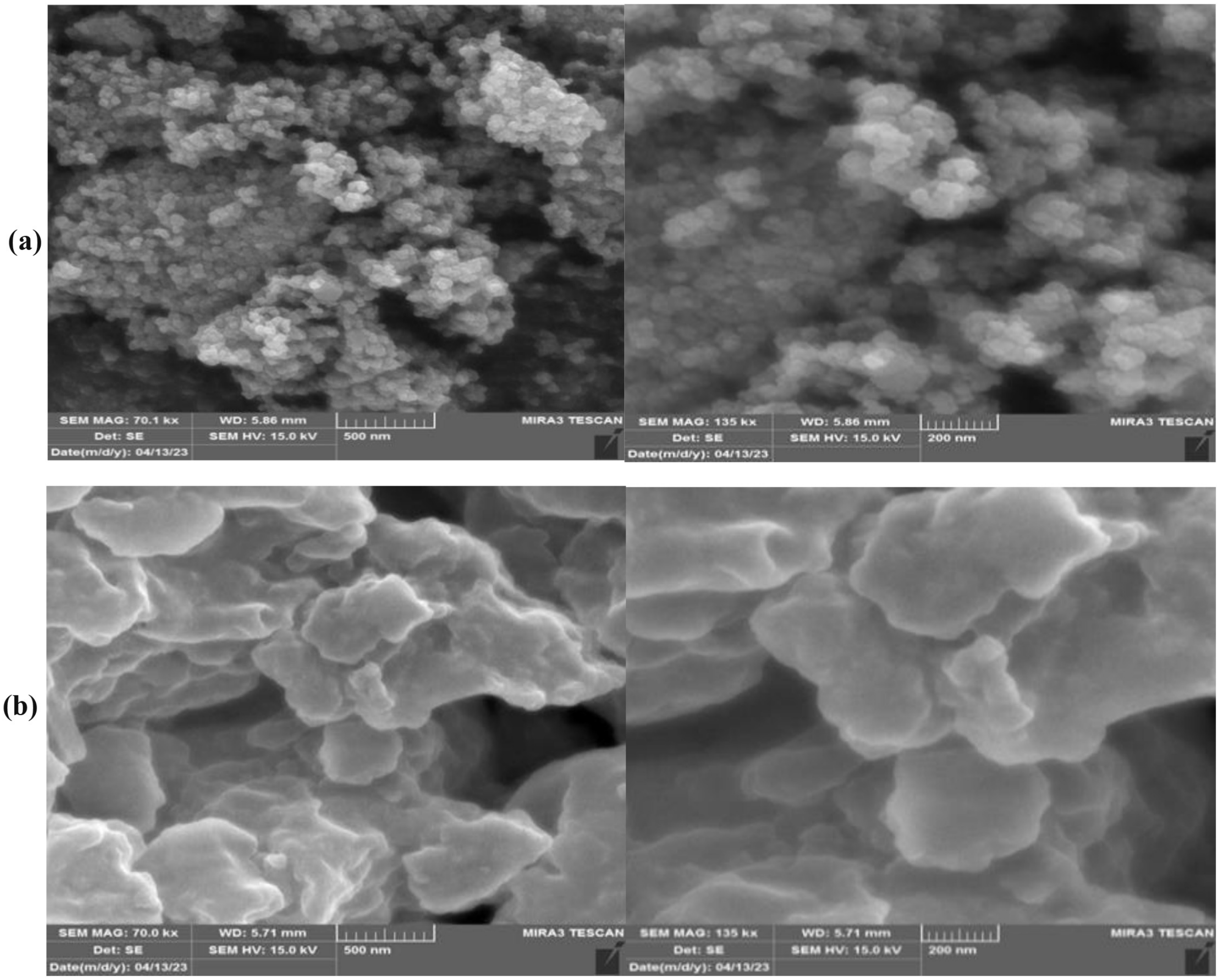

Fig. 2. FESEM images of (a) TiO_2 and (b) CQDs.

EDS spectra were used in the elemental analysis of the chemical compounds that were added to the prepared material. The EDS spectra of the synthesized TiO_2 NPs are displayed in Fig. 3. Titanium and oxygen are the elements that can be found in the TiO_2 NPs that were synthesized. These findings were consistent with those found in another research.[41] The percentage of Ti present in TiO_2 NPs was relatively high in comparison with the amount of oxygen present. The atomic and weight percentages of TiO_2 are tabulated in Fig. 3a. The elements present in the synthesized CQDs were carbon (C) and oxygen (O), these results were in agreement with other studies.[34,40] The atomic and weight percentage of CQDs are shown in the table inside Fig. 3b.

High-resolution transmission electron microscopy analysis

High-resolution transmission electron microscopy (HR-TEM) was conducted to examine the microstructure of the prepared materials. The HRTEM images of TiO_2 NPs and CQDs are presented in Fig. 4. Fig. 4a It shows that the TiO_2 NPs were agglomerated into small spherical shapes stacked together, and the scale of the image was at 50 nm. The grain size was calculated and the results showed that it is less than 15 nm. This result was confirmed by our XRD measurements in terms of particle size. As shown above, the crystal size from XRD was 15.89 nm, which was consistent with the HRTEM images. Fig. 4b shows that the scale of the image at 10 nm and the lattice fringes were calculated to be 0.31 nm.

HR-TEM images of CQDs are shown in Fig. 4(c) and Fig. 4(d) and the scale of the images was at 5 nm. Fig. 4(c) shows that the diameter of the CQDs was relatively uniform, and it had a dot spherical shape with highly crystalline structure and size below 5 nm. These results supported our XRD data on particle size. As shown above, the crystal size from XRD is 1.28 nm which was consistent with our HR-TEM images. Fig. 4(d) shows that the lattice spacing of

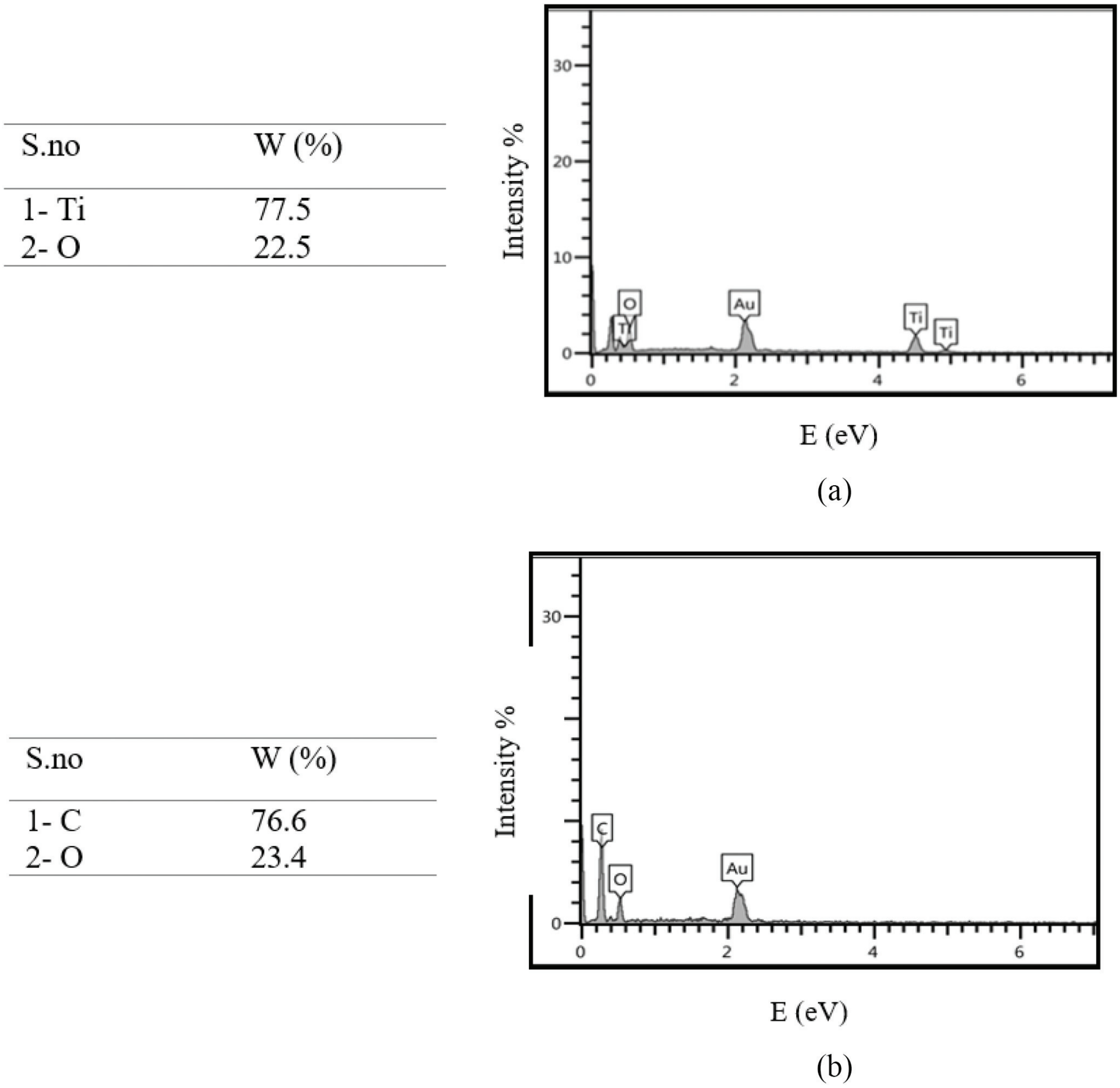

S.no	W (%)
1- Ti	77.5
2- O	22.5

(a)

S.no	W (%)
1- C	76.6
2- O	23.4

(b)

Fig. 3. (a) EDS spectra of TiO_2. (b) EDS spectra of CQDs.

CQDs was 0.24 nm. Fig. 5 shows histogram particle size distribution of TiO_2 NPs and CQDs.

Fourier transform infrared spectroscopy analysis

Fourier transform infrared (FTIR) spectro-scopy was carried out to gain an understanding of the interaction between NPs and capping agents. The FTIR spectra of TiO_2 NPs, CQDs, and TiO_2-CQDs nanocomposites showed the presence of a broad band at 450–4000 cm^{-1}, which was attributed to the stretching vibration of termi-nating hydroxyl groups in samples. The spectra of TiO_2 NPs displayed prominent peaks at 459, 826, 1324, 1616, and 3371 cm^{-1}, as shown in Fig. 6(a). The peaks at 459, 826, 1324, 1616 and 3371 cm^{-1} corresponded to Ti–O stretching, Ti–O–Ti stretching, C-H bending, C=O stretching, and O=H stretching, respectively, which were in agreement with the results.[42] These peaks were in agreement with the results.[34,35] Table 2 show that the FTIR spectrum of the TiO_2-CQDs nanocomopsites with different weight ratios was consistent with the results.[31] The wavenumbers of the absorption bands of the TiO_2-CQDs nano-comopsites were determined. Compared with pristine TiO_2, some new functional groups were observed in CQDs-modified TiO_2. The new peaks due to C-O-C streching, C=C stretching and C=H streching were ascribed to the addition of CQDs.[31]

Optical studies

The UV-visible and near-infrared absorbation spectra in the range of 200–900 nm were used to

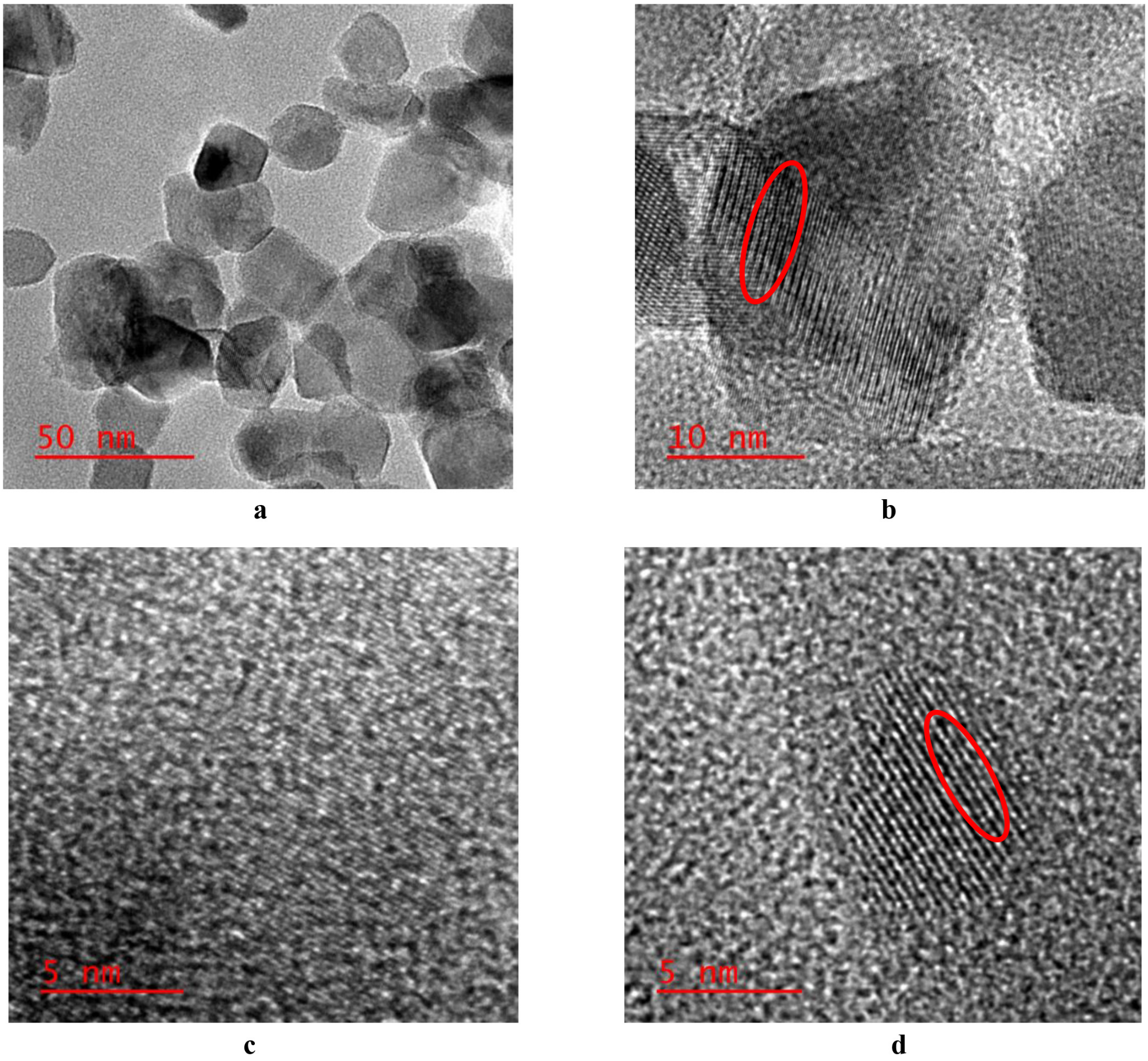

a b c d

Fig. 4. HR-TEM images of TiO_2 (a,b) and CQDs (c,d).

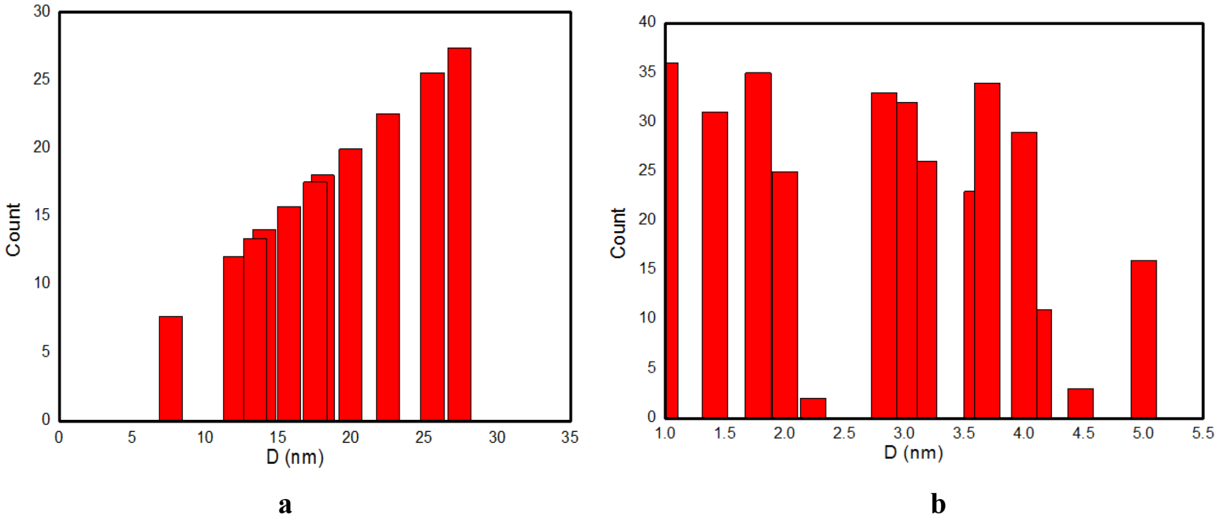

a b

Fig. 5. Histogram particle size distribution of TiO_2 (a) and CQDs (b).

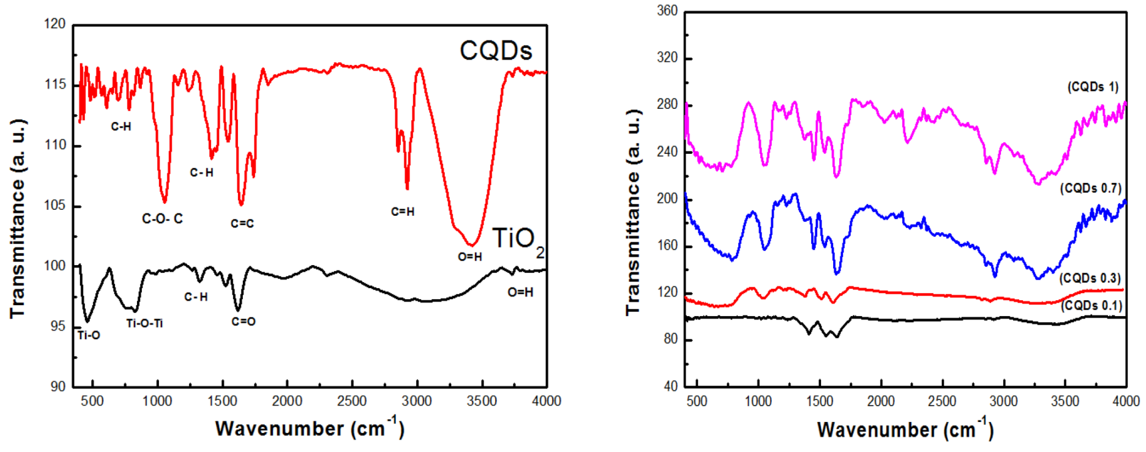

(a) (b)

Fig. 6. FTIR spectra of TiO_2 and CQDs (a) and TiO_2-CQDs nanocomposite (b).

Table 2. Wavenumbers of the absorption bands of the TiO_2-CQDs nanocomposite with increasing CQDs rate.

Vibrational bands	0.1	0.3	0.7	1
Ti-O stretching	420	432	458	463
C-O-C stretching	1018	1049	1060	1066
C-H bending	1411	1413	1454	1456
C=C stretching	1635	1639	1636	1642
C=H stretching	2878	2920	2927	2927
O-H stretching	3433	3271	3275	3287

investigate the optical properties of the materials that were prepared. The absorbance spec-tra of TiO_2 NPs, CQDs, and TiO_2-CQDs nanocomopsite are shown as a function of the wavelength in Fig. 7. The absorbance of TiO_2 rapidly decreased within the wavelength range of 200–400 nm. After this region, it decreased slowly with the increase in wavelength. After this region, it decreased slowly as the wavelengths increased. We found that the absorbance of TiO_2-CQDs nanocomposites incre-ased with the increase in the CQDs rate due to the upconversion photoluminescence (UCPL) property.[30] These results were in agreement with findi-ngs of other studies.[31] The values of the optical energy gap (Eg) were determined by using Tauc's relation, which is expressed as follows:[36]

$$\alpha h\upsilon = B_{\circ}\left(h\upsilon - E_g^{opt}\right)^{r} \qquad (8)$$

where hv denotes the photon energy, and B denotes a constant that does not depend on photon energy and r has four numeric values, (1/2) for allowed direct, 2 for allowed indirect, 3 for forbidden direct and (3/2) for forbidden indirect optical transitions.[36]

Fig. 8 shows the plot of $(\alpha h\upsilon)^2$ versus $h\upsilon$, and the energy gap (Eg) was calculated by using the absorption coefficient values and Tauc's equation by

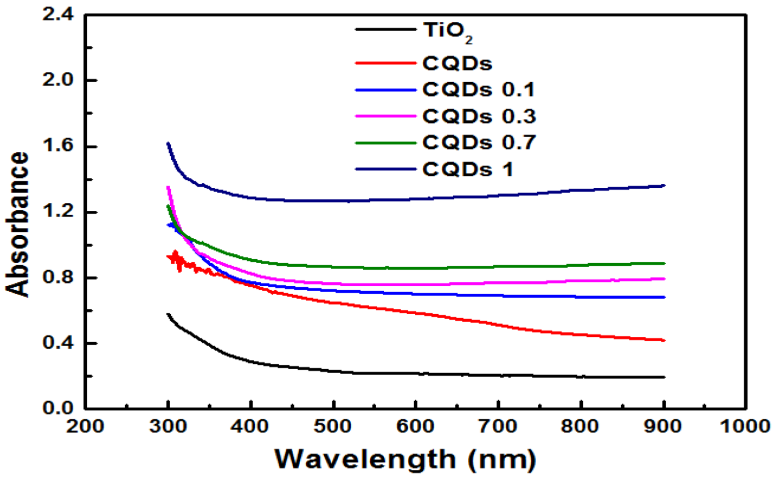

Fig. 7. Absorption spectra of the TiO_2, CQDs and TiO_2-CQDs nanocomopsite.

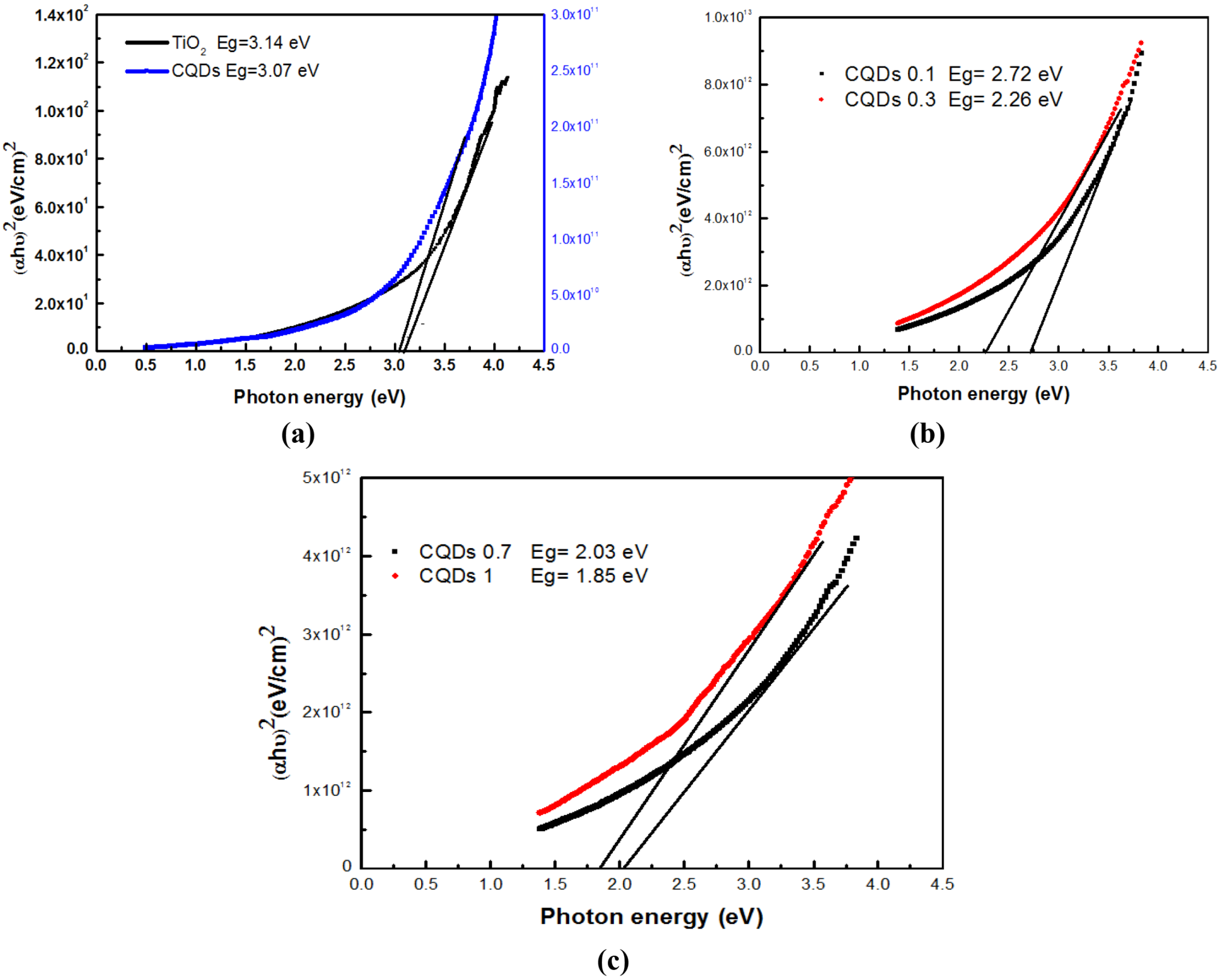

Fig. 8. Tauc plot of (a) TiO_2, (b) CQDs and (c) TiO_2-CQDs nanocomposite.

assuming allowed direct transition between valance and conduction bands. The energy band gap of TiO_2 was found to be 3.14 eV, which was in agreement with the value reported in the literature.[43] The energy band gap of CQDs was 3.07 eV, which was consistent with the results.[44,45] The energy band gap values of the TiO_2-CQDs nanocomposites decreased with increasing CQDs rate which was in agreement with the results.[30] The values of the optical energy gap were (2.72, 2.26, 2.03 and 1.85) eV for (CQDs 0.1) (CQDs 0.3) (CQDs 0.7) and (CQDs 1) respectively, These findings suggested that the small band gap and upconversion of CQDs might improve the capacity of TiO_2 to absorb visible light. This type of modification was distinct from the doping of carbon elements, which involves adding carbon atoms to the interface and surface lattice of TiO_2 to create an energy state that causes the material to absorb visible light.[30]

Photocatalytic studies

Figs. 9 and 10 illustrate how the UV–Vis absorption spectra of aqueous solutions containing 10 mg/L MB and MO changed as a function of the irradiation time. This change was caused by the photodegradation of TiO_2 NPs and TiO_2-CQDs nanocomposites that had different weight ratios. As a function of the amount of time that the sample was exposed to UV light, the characteristic absorption peaks of MB (664 nm) and MO (473 nm) were monitored. When the irradiation time was increased from 0 min to 240 min, the intensity of the absorption peaks experienced a significant reduction. In accordance with the finding.[30]

The absorbance of TiO_2-CQDs nanocomposites increased with the increase in the CQDs rate due to the up-conversion photoluminescence (UCPL) property.[30] Table 3 displays the percentage of photocatalyst samples that were effective in causing

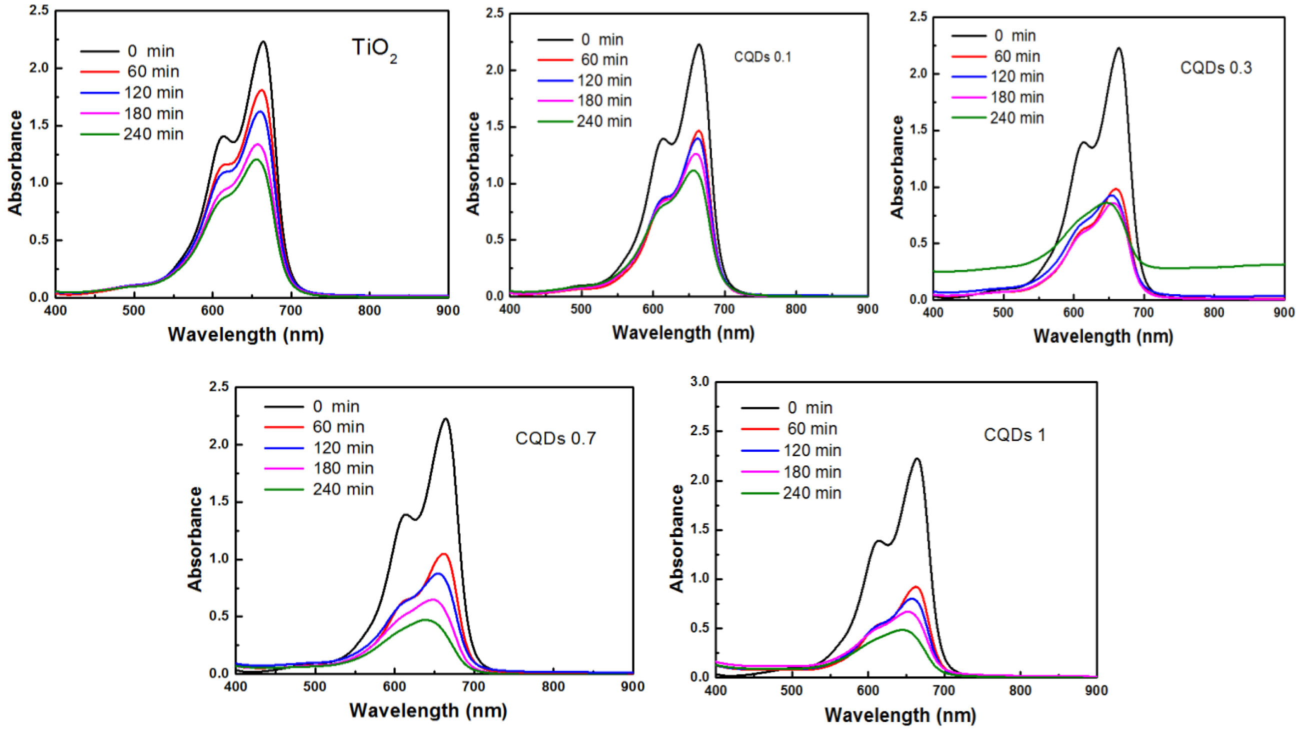

Fig. 9. UV-Vis absorption spectra of the photocatalytic degradation of MB for TiO_2 and TiO_2-CQDs nanocomposite.

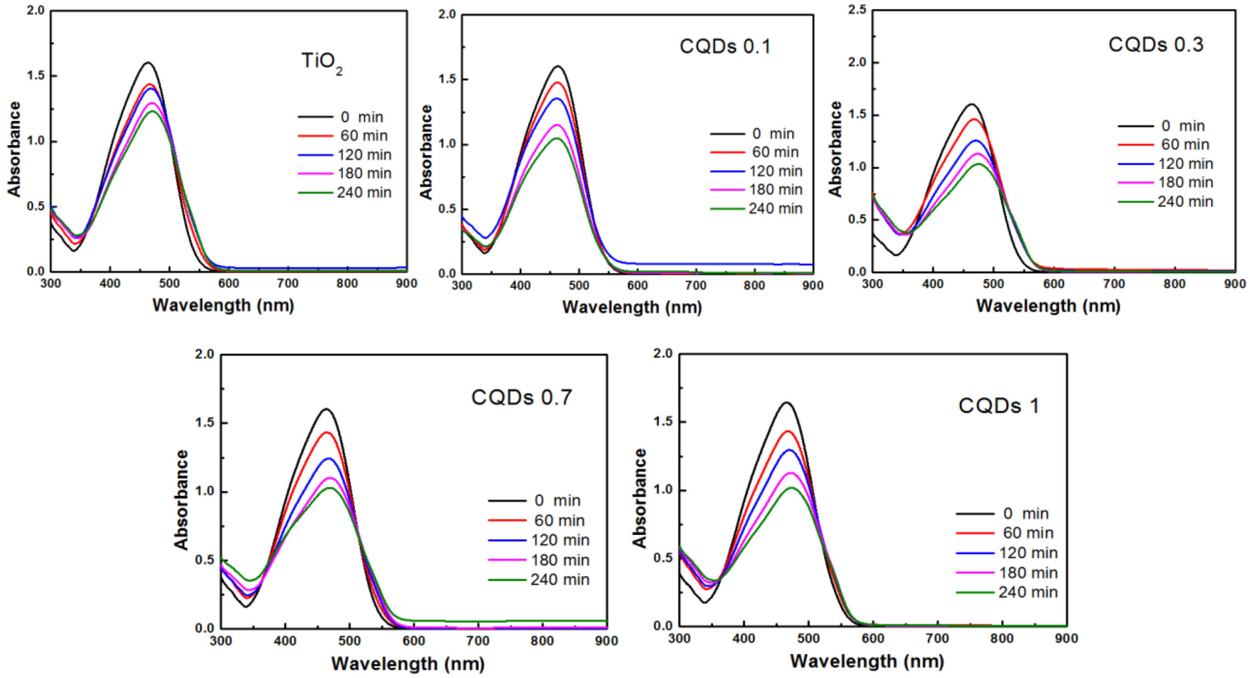

Fig. 10. UV-Vis absorption spectra of the photocatalytic degradation of MO for TiO_2 and TiO_2-CQDs nanocomposite.

Table 3. Efficiency values of TiO_2 and TiO_2-CQDs nanocomposite.

Dyes	TiO_2	CQDs 0.1	CQDs 0.3	CQDs 0.7	CQDs 1
MB	48%	52%	66%	73%	84%
MO	24%	29%	34%	36%	39%

degradation. The photocatalytic efficiency of all of the samples was significantly higher than that of pure TiO_2 NPs. Fig. 11 depicts the time dependent photodegradation of MB and MO dyes, and the results showed that the decomposition of MB and MO dyes

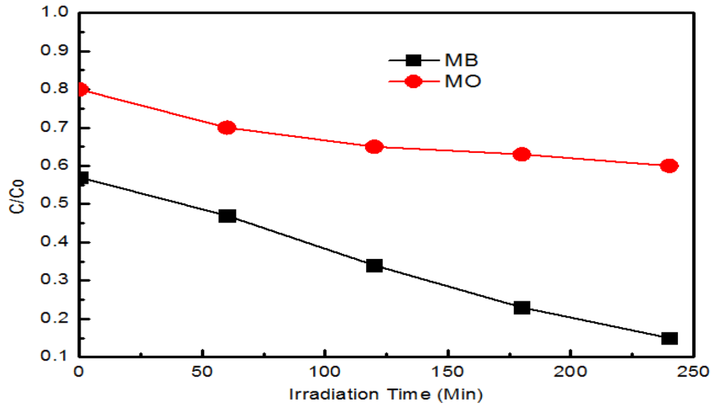

Fig. 11. Time-dependent photodegradation of MB and MO under.

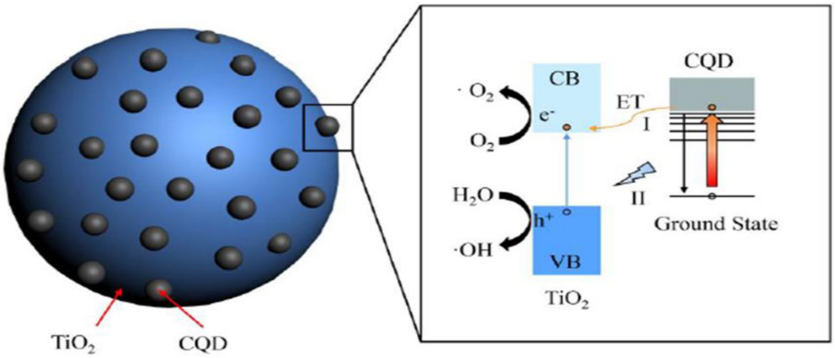

Fig. 12. Proposed mechanism for the photocatalytic process over TiO_2-CQDs.

increased as the time increased. According to our definition of the heterojunction mechanism, the creation of a heterojunction between CQDs and TiO_2 is responsible for the increased photocatalytic activity when exposed to UV light. The quantum confinement effect and surface oxygen-containing functional groups give CQDs a unique up conversion capability. As a result of this property, CQDs have the potential to absorb photons with low energies and emit photons with high energies. When CQDs are coupled with TiO_2, two mechanisms of energy transfer between CQDs and TiO_2 take place when nanosized CQDs anchor on the surface of TiO_2. By exposing the TiO_2-CQDs combination to UV radiation, the CQDs are activated by high energy photons and create electrons and holes. The production of superoxide radicals is mostly aided by the photoinduced electrons, which move from the excited state to the conduction band of TiO_2, the holes produced hydroxyl radicals and remained in their ground states,[30] as seen in the illustration (step I) in Fig. 12.

UV light irradiation

Meanwhile, the remainder of the uv light's photons with low energies was absorbed by the CQDs, which resulted in the production of electron-hole pairs. These electron-hole pairs then recombined at the ground state of the CQDs, which caused the CQDs to emit photons with high energies due to the up-conversion properties of the CQDs.[30] Subsequently, photons with a high energy could excite the TiO_2 host and produce electron-hole pairs for the photocatalytic reaction, as shown in step II of Fig. 12. Thus, the up-conversion process has the potential to further increase the efficiency with which UV light is utilized. In addition, the oxygen-containing groups exert some degree of influence over the efficiency with which electrons are transferred from CQDs to TiO_2 because the electronegativity of functional groups can change depending on the conditions of the reaction. This relationship can have an effect on the amount of hydroxyl and superoxide radicals that are produced,[30] followed by the breakdown of MB and MO dyes. The reactions can be summarized as follows in their shortened form:

$$\text{sample} + h\nu\,(\text{eV}) \rightarrow e^-\,(\text{CB}) + h^+\,(\text{VB}) \quad (9)$$

$$e^- + O_2 \rightarrow {}^{\cdot}O_2^- \quad (10)$$

$$H^{+} + O_2 \rightarrow {}^{\cdot}OH^{-} \tag{11}$$

$${}^{\cdot}O_2{}^{-} + \text{dye molecule} \rightarrow \text{degradation products} \tag{12}$$

$$OH^{-} + \text{dye molecule} \rightarrow \text{degradation products} \tag{13}$$

Conclusion

In this research, the utilization of TiO_2-based photocatalytic for UV light has improved by maximizing the ability of water-soluble CQDs for up conversion. For the results, XRD showed that the CQDs exhibited a broad peak at (002) with hexagonal structure, and TiO_2 (anatase phase) had a polycrystalline nature with tetragonal structure. The FESEM results showed the formation of nanostructures with different shapes and small average particle sizes. HR-TEM revealed that the TiO_2 (anatase phase) agglomerated in mostly spherical shapes and size less than 15 nm, the CQDs had a relatively uniform diameter, a spherical shape with a highly crystalline structure, and a size below 5 nm. The results of UV-visible spectroscopy showed that the absorbance of TiO_2-CQDs nanocomposite increased with the increase in the CQDs rate, and the optical energy band gap of TiO_2 and CQDs was 3.14 and 3.07 eV, respectively. The energy band gap values of TiO_2-CQDs nanocomposite decreased with the increase in the CQDs rate in the range of (1.85–2.72) eV And CQDs that were manufactured were verified to possess obvious up conversion properties that could transform low energy photons into high-energy photons. As a result, the incorporation of CQDs played a critical role in broadening the light response range and increasing the quantum yield. Under the influence of UV light, the photocatalytic activity of each sample was superior to that of pure TiO_2. Within 240 min, the efficiency of the breakdown of MB and MO was extremely high at 84% and 39% respectively. Following the completion of data analysis, we proposed a workable model to explain the photocatalytic process, which takes place when UV light is present. Thus, CQDs, which are composed of carbon materials, offer a novel strategy for the development of excellent and nontoxic catalysts.

Authors' declaration

- Conflicts of Interest: None.
- We hereby confirm that all the Figures and Tables in the manuscript are ours. Furthermore, any Figures and images, that are not ours, have been included with the necessary permission for republication, which is attached to the manuscript.
- No animal studies are present in the manuscript.
- No human studies are present in the manuscript.
- Ethical Clearance: The project was approved by the local ethical committee at University of Diyala.

Authors' contribution statement

M. S. J., O. A. M., Z. N. J. and N. J. J. contributed to the design and implementation of the research, to the analysis of the results and the writing of the manuscript.

References

1. Damjan B, Julio C, Nikola K, Andrea J, Janez Z, Ander J, *et al.* Photodegradation of methylene blue and rhodamine B using laser-synthesized ZnO nanoparticles. J Mater. 2020 Sep;13(19):4357. https://doi.org/10.3390/ma13194357.
2. Al-Rawi KR, Taha SK. The effect of nano particles of TiO_2-Al_2O_3 on the mechanical properties of epoxy hybrid nanocomposites. Baghdad Sci J. 2015 Sep;6;12(3):597–602. https://doi.org/10.21123/bsj.2015.12.3.597-602.
3. Catalina N D, Consuelo G D, Gabriela A, Apostolescu G C, Doina L, Lidia F, *et al.* Enhancing the TiO_2-Ag photocatalytic efficiency by acetone in the dye removal from wastewater. Water. 2022 Agu;14(17):2711. https://doi.org/10.3390/w14172711.
4. Subramanian K. Radhakrishnan V. Photocatalytic degradation of organic dyes by PEG and PVP capped Cu, Ni and Ag nanoparticles in the presence of $NaBH_4$ in aqueous medium. J Water Environ Nanotechnol. 2020 Aut;5(4):294–306. https://doi.org/10.17577/IJERTCONV4IS03004.
5. Ahmed M, Ibrahim M, Moustafa SA, Ehab KE, Khalaf F, Mohamed S, *et al.* Advanced oxidation processes usingzinc oxide nanocatalyst for detoxification of some highly toxic insecticides in an aquatic system combined with improving water quality parameters. Front Environ Sci. 2022 Mar;10:1–14. https://doi.org/10.3389/fenvs.2022.807290.
6. Saadiyah AD, Enass AH, Asaad HS, Mouna S. Removal color study of toluidine blue dye from aqueous solution by using photo-fenton oxidation. Baghdad Sci J. 2016;(2s(Supplement));13:440–446. https://doi.org/10.21123/bsj.2016.13.2.2NCC.0440.
7. Mahendra K, Jean MF, Brian JF, Bindu K, Ramesh KP. Photocatalytic degradation of organic textile dyes using tellurium-based metal alloy. Vacuum. 2022 May;199:110960. https://doi.org/10.1016/j.vacuum.2022.110960.
8. Abdessalam B, Brahim A, Elhassan A, Bahcine B, Aziz T, Sylvie V, *et al.* Photo degradation under UV light irradiation of various types and systems of organic pollutants in the presence of a performant $BiPO_4$ photocatalyst. J Catalysts. 2022 Jun;12:3–19. https://doi.org/10.3390/catal12070691.
9. Noor AM, Abeer IA, Mohammed SS. Photocatalytic degradation of reactive yellow dye in wastewater using H_2O_2/TiO_2/UV. Technique. Iraqi J Chem Pet Eng. 2020 Mar;21(1):15–21. https://doi.org/10.31699/IJCPE.2020.1.3.
10. Zimi SC, Shirini F. Advanced oxidation process as a green technology for dyes removal from wastewater: A review. Iran J Chem Chem Eng. 2021 Sep;40(5):1467–1489. https://doi.org/10.30492/ijcce.2020.43234.

11. Dorcas M, Raymond T, Taziwa Lindiwe K. Antibacterial and photodegradation of organic dyes using lamiaceae-mediated ZnO nanoparticles: A review. Nanomaterials. 2022 Des;12:4469. https://doi.org/10.3390/nano12244469.
12. Padmavathy N, Narasimha BM, Hemakumar KH. Direct sunlight driven photocatalytic degradation of hazardous organic dyes using TiO_2-NiO nanocomposite p-n junction. J Phy Conf Ser. 2021 Aug;2070:012044. https://doi.org/10.1002/jctb.1553.
13. Santiago E, Daniele MB, Luiz Gustavo TK, Márcia D. Ozonation and advanced oxidation technologies to remove endocrine disrupting chemicals (EDCs) and pharmaceuticals and personal care products (PPCPs) in water effluents. J Hazard Mater. 2007 Nov;149(3):631–642. https://doi.org/10.1016/j.jhazmat.2007.07.073.
14. Johnson M B, Mehrvar M. Aqueous metronidazole degradation by UV/H_2O_2 process in singleand multi-lamp tubular photoreactors: Kinetics and reactor design. Ind Eng Chem Res. 2008 Aug;47(17):6525–6537. https://doi.org/10.1021/ie071637v.
15. Peternel I, Koprivanac N. Kusic H. UV-based process for reactive azo dye mineralization, J Water Res. 2006 Feb;40(3):525–532. https://doi.org/10.1016/j.watres.2005.11.029.
16. Murugandham M, Swaminathan M. Photochemical oxidation of reactive azo dye with UV-H_2O_2 process. Dyes Pigm. 2004 Sep;62(3):269–275. https://doi.org/10.1016/J.DYEPIG.2003.12.006.
17. Carla A Silva, Luis M. Madeira, Rui A. Boaventura, Carlos A. Costa. Photo-oxidation of cork manufacturing wastewater. Chemosphere. 2004;55:19. https://doi.org/10.1016/j.chemosphere.2003.11.018.
18. Souad AM, Sanaa T, Eman AM. Studying the photodegradation of congo red dye from aqueous solutions using bimetallic Au–Pd/TiO_2 Photocatalyst. Baghdad Sci J. 2021 Des;18(4):1261–1268. http://dx.doi.org/10.21123/bsj.2021.18.4.1261.
19. Ghoreishi SM, Haghighi R. Chemical catalytic reaction and biological oxidation for treatment of the of non-biodegradable textile effluent. J Chem Eng. 2003 Sep;95(1–3):163–169. https://doi.org/10.1016/S1385-8947(03)00100-1.
20. Vetriselvan K, Sudhagar P, Ajay KK, Gomathipriya P. Photocatalytic degradation of synthetic organic reactive dye wastewater using GO-TiO_2 Nanocomposite. Pol J Environ Stud. 2020 Apr;29(2):1683–1690. https://doi.org/10.15244/pjoes/109027.
21. Luiz EN, Eduardo CM, Helton JA, Marco AR, Erika CV, Leda MS. Braz Arch Biol Technol. 2020;63:1–15. https://doi.org/10.1590/1678-4324-2020180573.
22. Yi-Hsuan C, Tso-Fu MC, Chun-YC, Masato S, Yung JH. Mechanistic insights into photodegradation of organic dyes using heterostructure photocatalysts. Catalysts 2019 May;9(5):430. https://doi.org/10.3390/catal9050430.
23. Deivanai SK, Kanmani S. Photocatalytic degradation of reactive dyes and real textile composite wastewater using TiO_2/MWCNT nanocomposite under UVA and UVA-LED irradiation. A comparative study. J Environ Prot Eng. 2019 May;45:95–116. https://doi.org/10.5277/epe190207.
24. Ganjar F, Muhamad AS. Preliminary study of photocatalytic degradation of methylene blue dye using magnetic Alginate/Fe_3O_4 (Alg/Fe_3O_4) Nanocomposites. Eksakta: Int J Data Sci Anal. 2019 Jan;19(1):26–34. https://doi.org/10.20885/eksakta.vol19.iss1.art3.
25. Galindo C, Kalt A. UV/H_2O_2 oxidation of monoazo dyes in aqueous media: a kinetic study. Dyes Pigm. 1998 Jan;40(1):27–35. https://doi.org/10.1016/S0143-7208(98)00027-8.
26. Mustafa MK, Abbas WS, Ameerah MZ, Wesam RK. Inhibition of SARS-CoV-2 reproduction using boswellia carterii: A theoretical study. J Mole Liq. 2021 Sep;337:116440. https://doi.org/10.1016/j.molliq.2021.116440.
27. Noor AK, Mustafa MK, Anees AK. Effect of trimethoprim drug dose on corrosion behavior of stainless steel in simulated human body environment: Experimental and theoretical investigations. J Bio Tribo-Corros. 2021 Sep;7(124):1–15. https://doi.org/10.1007/s40735-021-00559-8.
28. Ayodeji OI, Akeem AO, Mustafa G. Sun-light driven enhanced azo dye decontamination from aqueous solution. Desalin Water Treat. 2020 Feb;177:423–4304. https://doi.org/10.5004/dwt.2020.25247.
29. Sahani S, Sharma YC. Advancements in applications of nanotechnology in global food industry. Food Chem. 2021;342:128318. https://doi.org/10.1016/j.foodchem.2020.128318.
30. Negi G, Anirbid S, Sivakumar P. Applications of silica and titanium dioxide nanoparticles in enhanced oil recovery: Promises and challenges. J Pet Sci Res. 2021;6(3):224–46. https://doi.org/10.1016/j.ptlrs.2021.03.001.
31. Shaker DS, Abass NK, Ulwall RA. Preparation and study of the structural, morphological and optical properties of pure tin oxide nanoparticle doped with Cu. Baghdad Sci J. 2022;19(3):0660. https://doi.org/10.21123/bsj.2022.19.3.0660.
32. Visaveliya NR, Mazetyte-Stasinskiene R, Köhler JM. Stationary, continuous, and sequential surface-enhanced raman scattering sensing based on the nanoscale and microscale polymer-metal composite sensor particles through microfluidics: A review. Adv Opt Mater. 2022:2102757. https://doi.org/10.1002/adom.202102757.
33. Pourpasha H, Zeinali Heris S, Mohammadfam Y. Comparison between multi-walled carbon nanotubes and titanium dioxide nanoparticles as additives on performance of turbine meter oil nano lubricant. Sci Rep. 2021;11(1):1–19. https://doi.org/10.1038/s41598-021-90625-5.
34. Hakeem HS, Abbas NK. Preparing and studying structural and optical properties of Pb_1-xCdxS nanoparticles of solar cells applications. Baghdad Sci J. 2021;18(3):0640. https://doi.org/10.21123/bsj.2021.18.3.0640.
35. Hano C, Abbasi BH. Plant-Based green synthesis of nanoparticles: production, characterization and applications. Biomolecules. 2021;12(1):31. https://doi.org/10.3390/biom12010031.
36. Grujić-Brojčin M, Šćepanović M, Dohčević-Mitrović Z, Popović Z. Infrared study of nonstoichiometric anatase TiO_2 nanopowders. Sci Sinter. 2006;38(2):183–9. https://doi.org/10.2298/SOS0602183G.
37. Rahma A, Oleiwi H, Khaleel S, Mutter M, editors. Morphology, structure, and optical properties of ZnO nanorods/Eosin-y grown via microwave-assisted hydrothermal method. IOP Conf Ser: Mater Sci Eng. 2021;1095:012007: IOP Publishing. https://doi:10.1088/1757-899X/1095/1/012007.
38. Kozuka H, Kuroki H, Sakka S. Flow characteristics and spinnability of sols prepared from silicon alkoxide solution. J Non Cryst Solids 1988;100(1–3):226–30. https://doi.org/10.1016/0022-3093(88)90022-1.
39. Iravani S. Green synthesis of metal nanoparticles using plants. Green Chem. 2011;13(10):2638–50. https://doi:10.1039/C1GC15386B.

40. Hassan AK, Atiya MA, Luaibi IM. A green synthesis of iron/copper nanoparticles as a catalytic of fenton-like reactions for removal of orange G dye. Baghdad Sci J. 2022;19(6):1249–1264. https://doi.org/10.21123/bsj.2022.6508.
41. Rao KG, Ashok C, Rao KV, Chakra CS, Rajendar V. Synthesis of TiO_2 nanoparticles from orange fruit waste. Int J Adv Multidiscip Res. 2015;2(1):1. https://doi.org/10.1039/C1GC15386B.
42. Davar F, Majedi A, Mirzaei A. Green synthesis of ZnO nanoparticles and its application in the degradation of some dyes. J Am Ceram Soc. 2015;98(6):1739–46. https://doi.org/10.1111/jace.13467.
43. Girisuta B, Janssen L, Heeres H. A kinetic study on the decomposition of 5-hydroxymethylfurfural into levulinic acid. Green Chem. 2006;8(8):701–9. https://doi.org/10.1039/B518176C.
44. Rao KG, Ashok C, Rao KV, Chakra C, Tambur P. Green synthesis of TiO_2 nanoparticles using Aloe vera extract. Int J Adv Res Phys Sci. 2015;2(1A):28–34. https://doi.org/10.1080/17518253.2018.1538430.
45. Amanulla AM, Sundaram R. Green synthesis of TiO_2 nanoparticles using orange peel extract for antibacterial, cytotoxicity and humidity sensor applications. Mater Today: Proc. 2019;8:323–331. https://doi.org/10.1016/j.matpr.2019.02.118.

تطبيقات التحفيز الضوئي للمركبات النانوية TiO_2-CQDs المحضرة بالطرق البيولوجية

مريم ستار جبار[1]، ألفت أحمد محمود[1] ،زينب ناصر جميل[2]، نور جمال جهاد [2]

[1]علوم الفيزياء، كلية العلوم ، جامعة ديالى ، ديالى العراق.
[2]هندسة الاتصالات، كلية الهندسه، الجامعة التكنولوجيه، بغداد، العراق.

الخلاصة

في هذه الدراسة ، تم تصنيع CQDs بالطريقة الخضراء بأستخدام عصير البرتقال والايثانول تم خلطها عند درجة حرارة منخفضة نسبيا بواسطة عملية الكربنة الحرارية المائية، وتم تحضير حبيبات TiO_2 بواسطة طريقة sol-gel. وكذلك تم تحضير المركبات النانوية و TiO_2-CQDs بنسب وزنية مختلفة بواسطة الخلط الانزلاقي والمعالجة الحرارية. أظهرت نتائج FESEM تكوين مواد نانوية بأشكال مختلفة وبمعدل حجم حبيبي صغير كشف المجهر الإلكتروني النافذ عالي الدقة أن TiO_2 طور (anatase) يتجمع في أشكال وأحجام كروية في الغالب أقل من 15 nm. كان لنقاط الكميات الكمية قطر موحد نسبيًا، وشكل كروي ذو بنية بلورية عالية، وحجم أقل من 2 nm. تُظهر أطياف FTIR للمواد النانوية المحضرة وجود النطاق العريض عند cm^{-1} (450–4000)يتوافق مع اهتـزاز التمدد لمجموعات الهيدروكسيل المنتهية في العينات. أظهرت نتائج التحليل الطيفي المرئي للأشعة فوق البنفسجية أن امتصاصية المتراكبات النانوية (TiO_2-CQD) تزداد مع زيادة نسبة CQDs ، وكانت قيمة فجوة الطاقة البصرية 3.14 eV و 3.07 eV للمواد TiO_2 و CQDsعلى التوالي. وانخفضت قيم فجـوة الطاقة للـمتراكبات TiO_2-CQDsالنانـوية مع زيادة معدل CQDs ضمن المدى eV (1.85–2.72) . تم اختبار أداء التحفيز الضوئي عن طريق تحلل صبغات الميثيلين الأزرق (MB) والميثيل البرتقالي (MO) تحت تأثير إشعاع الأشعة الفوق البنفسجية. أظهرت النتائج أن جميع المواد المتراكبة المحضرة بنسب مختلفة كانت لها كفاءة تحفيزية ضوئية أعلى من TiO_2 NPs ، وأن كفاءة التحفيز الضوئي تزداد مع زيادة نسبة CQDs . كانت كفاءة التحلل لكل من الميثيلين الأزرق (MB) والميثيل البرتقالي (MO) عند 84% و 39 % عند 240دقيقة على التوالي.

الكلمات المفتاحية: الاناتاز، نقاط الكاربون المكممة، المجهر الالكتروني الباعث للمجال، المجهر الالكتروني النافذ عالي الدقة، ثنائي اوكسيد التيتانيوم، حيود الاشعة السينية.